

The Fengyun-4B Digital Fluxgate Magnetometer

Chenghan Weng¹, Bin Zhou², Yongliang Xue¹, Yuqi Tong³, Bingjun Cheng², Yiteng Zhang⁴, Jingdong Wang², Lei Li², Xin Zhang², Ruyi Zhang⁵, Liguang Zhang⁵, Jianguang Guo⁶, Weiguo Zong⁶, Bo Chen⁶, Xiaoxin Zhang⁷, and Jingsong Wang⁶

¹1. State Key Laboratory of Space Weather, National Space Science Center, Chinese Academy of Sciences 2. Key Laboratory of Solar Activity and Space Weather, National Space Science Center, Chinese Academy of Sciences

²National Space Science Center, Chinese Academy of Sciences

³1. State Key Laboratory of Space Weather, National Space Science Center, Chinese Academy of Sciences 2. Key Laboratory of Solar Activity and Space Weather, National Space Science Center, Chinese Academy of Sciences 3. School of Astronomy and Space Science, University of Chinese Academy of Sciences

⁴Center for Space Science and Applied Research, Chinese Academy of Sciences

⁵Shanghai Institute of Satellite Engineering

⁶National Center for Space Weather, China Meteorological Administration

⁷China Meteorological Administration

December 15, 2022

Abstract

This paper describes the development of the fluxgate magnetometer on the Fengyun-4B satellite. The Fengyun-4 is the second generation of China's geostationary orbit satellite with the function of monitoring the space environment in GEO orbit. A fluxgate magnetometer (FGM) is deployed on this satellite to observe the magnetic field as a necessary input to space weather forecasting. This payload adopts three 3-axis fluxgate sensors to obtain space magnetic field data by excluding the satellite's interference. Each three-axis fluxgate sensor has an independent signal processing circuit. FGM uses digital signal processing technology to acquire magnetic field signals. First, the analog signal is oversampled using a high-speed ADC, then digital signal processing, such as phase-sensitive demodulation, integration, and filtering, is performed inside the FPGA, and the feedback signal is output to the feedback coil through the DAC. This signal processing loop constitutes an ADC system, and the quantization accuracy of the output digital quantity can reach 18 bits. the FGM performs in-orbit calibration during satellite rotation maneuver and Alfvén wave events. Comparison with the GOES-16 satellite and Tsyganenko magnetic field model proves FGM to be effective in monitoring the magnetic field of the space environment. Through joint observations with GOES-16 satellite and geomagnetic stations, FY-4B describes the development of a typical magnetic storm on November 4, 2021. The Ground calibration and in-orbit preliminary results show the FY-4B satellite magnetometer outputs 20 bits of digital resolution data at a 30 Hz sampling rate, with the noise lower than $3 \times 10^{-4} \text{ nT}^2/\text{Hz}@1\text{Hz}$ in the $\pm 600 \text{ nT}$ range.

Hosted file

951636_0_art_file_10522469_rmms0z.docx available at <https://authorea.com/users/566471/articles/613168-the-fengyun-4b-digital-fluxgate-magnetometer>

1
2
3
4
5
6

7
8
9
10
11
12
13
14
15
16
17
18
19
20
21
22
23
24
25
26
27
28
29

The Fengyun-4B Digital Fluxgate Magnetometer

Cheng-Han Weng^{1,2}†, Bin Zhou^{1,2}†, Yong-Liang Xue^{1,2}, Yu-Qi Tong^{1,2,3}, Bing-Jun Cheng^{1,2},
Yi-Teng Zhang^{1,2}, Jin-Dong Wang^{1,2}, Lei LI^{1,2}*, Xin Zhang⁴, Ru-Yi Zhang⁵, Li-Guo
Zhang⁵, Jian-Guang Guo^{6,7}, Wei-guo Zong^{6,7}, Bo Chen^{6,7}, Xiao-Xin Zhang^{6,7}*, Jin-song
Wang^{6,7}

1. State Key Laboratory of Space Weather, National Space Science Center, Chinese Academy of Sciences, Beijing, China

2. Key Laboratory of Solar Activity and Space Weather, National Space Science Center, Chinese Academy of Sciences, Beijing, China

3. School of Astronomy and Space Science, University of Chinese Academy of Sciences, Beijing, China

4. Beijing Key Laboratory of Space Environment Exploration, National Space Science Center, Chinese Academy of Sciences, Beijing, China

5. Shanghai Institute of Satellite Engineering, Shanghai, China

6. Key Laboratory of Space Weather, National Satellite Meteorological Center (National Center for Space Weather), China Meteorological Administration, Beijing, China

7. Innovation Center for FengYun Meteorological Satellite (FYSIC), China Meteorological Administration, Beijing, China

*Corresponding author: Lei LI (lil@nssc.ac.cn) ; Xiao-Xin ZHANG (xxzhang@cma.gov.cn).

†Cheng-han Weng and Bin Zhou are co-first authors of the article

Key Points:

- The FY-4B magnetometer uses digital fluxgate technology with the $\Sigma - \Delta$ frame to realize digital quantization of magnetic field with high SNR.
- After ground calibration and in-orbit test, FY-4B FGM shows good performance in GEO orbital magnetic field monitoring
- The FY-4B magnetometer observations are comparable with the GOES-16 satellite, geomagnetic stations and magnetic field models.

30 Abstract

31 This paper describes the development of the fluxgate magnetometer on the Fengyun-4B satellite.
32 The Fengyun-4 is the second generation of China's geostationary orbit satellite with the function
33 of monitoring the space environment in GEO orbit. A fluxgate magnetometer (FGM) is deployed
34 on this satellite to observe the magnetic field as a necessary input to space weather forecasting.
35 This payload adopts three 3-axis fluxgate sensors to obtain space magnetic field data by
36 excluding the satellite's interference. Each three-axis fluxgate sensor has an independent signal
37 processing circuit. FGM uses digital signal processing technology to acquire magnetic field
38 signals. First, the analog signal is oversampled using a high-speed ADC, then digital signal
39 processing, such as phase-sensitive demodulation, integration, and filtering, is performed inside
40 the FPGA, and the feedback signal is output to the feedback coil through the DAC. This signal
41 processing loop constitutes an ADC system, and the quantization accuracy of the output digital
42 quantity can reach 18 bits. the FGM performs in-orbit calibration during satellite rotation
43 maneuver and Alfvén wave events. Comparison with the GOES-16 satellite and Tsyganenko
44 magnetic field model proves FGM to be effective in monitoring the magnetic field of the space
45 environment. Through joint observations with GOES-16 satellite and geomagnetic stations, FY-
46 4B describes the development of a typical magnetic storm on November 4, 2021. The Ground
47 calibration and in-orbit preliminary results show the FY-4B satellite magnetometer outputs 20
48 bits of digital resolution data at a 30 Hz sampling rate, with the noise lower than 3×10^{-4}
49 $\text{nT}^2/\text{Hz}@1\text{Hz}$ in the $\pm 600\text{nT}$ range.

50 Plain Language Summary:

51 As a meteorological satellite, the Fengyun-4B can monitor almost the entire Eastern Hemisphere
52 from the geostationary orbit, including the Earth's environment, and the space environment
53 around the Earth as well. The magnetic field observation is one of the tasks. The magnetic field
54 instrument adopts a new design, the signals of the sensors are digitized and processed by
55 software in the processor. This approach can enhance the instrument performance and reduce the
56 size of the instrument. This article describes the ground tests of the magnetometer. Through these
57 tests, the instrument's performance is fully evaluated, key parameters are calibrated, the
58 instrument is prepared for space observation. Now the magnetometer is operating in the
59 geosynchronous orbit. After comparing with the GOES-16 satellite and the magnetospheric
60 magnetic field model, we concluded that the Fengyun-4B magnetometer is working well in orbit.
61 During a solar storm, Fengyun-4B observed the onset, main phase and recovery of the storm,
62 allowing us to gain a deep understanding of the magnetic storm.

63 1 Introduction

64 The Fengyun-4 (FY-4) is the second generation of Chinese geosynchronous orbit meteorological
65 satellite. The FY-4A and FY-4B satellites were successfully launched in Xichang, China, in
66 December 2016 and June 2021, respectively. The FY-4 satellites are deployed with space
67 environment monitoring instrument packages to detect parameters of the space environment such
68 as magnetic fields, energetic particles, and radiation effects (Yang et al., 2017). Among them, the
69 magnetometer of the FY-4 satellite inherited the fluxgate magnetometer technology from the
70 YingHuo-1 fluxgate magnetometer (Zhou et al., 2009), which was also successfully applied to
71 the HPM of the CSES mission launched in February 2018 (Cheng et al., 2018). The
72 magnetometer signal of the FY-4A satellite is processed according to the traditional analog

73 signal processing method; while the FY-4B satellite magnetometer adopts the digital signal
74 processing technique.

75 Fluxgate digital signal processing techniques have been being developed rapidly in recent years
76 and widely used in space exploration. For example, digital fluxgate magnetometer technology is
77 used in space missions such as Astrid-2 (Erik et al., 1999), Venus Express (Zhang et al., 2007),
78 and BepiColombo (Glassmeier et al., 2010), where the input and output of analog signals are
79 realized using ADC and DAC, and the processing of signal demodulation is performed inside the
80 FPGA (Baumjohann et al., 2010). This technique has advantages over analog signal processing
81 techniques, in reducing the number of chips, and improving the radiation hardness. However, its
82 disadvantages are also obvious, the limited quantization accuracy of the DAC affects the
83 resolution and linearity of the instrument. The use of oversampling and sigma-delta technology
84 can improve the overall data quantization accuracy. In general, the overall magnetometer data
85 quantization bits can be increased by 2 to 4 bits compared to the DAC quantization bits. This
86 digital signal processing technology is currently mainly used in low magnetic field measurement.
87 In the GEO orbit where FY-4B operates, the magnetic field is generally within 200nT, which is
88 ideal for the application of digital fluxgate technology.

89 In this paper, the design and calibration of the digital fluxgate magnetometer (FGM) for the FY-
90 4B satellite will be presented in the following sections, respectively.

91 **2 Instrument Requirements**

92 Magnetic field detection in GEO enables the monitoring of the geomagnetic storms and
93 substorms, studying the solar wind interaction with the magnetosphere. Continuous magnetic
94 field observation for a long time is of great significance to the forecast of space weather and
95 scientific research.

96 In GEO orbit, the magnetic field is usually around 100~200nT. During the geomagnetic activity,
97 the magnetic field fluctuates considerably. Referring to the observation results of the GOES-16
98 satellite, and considering a certain design margin, the measurement range of FGM is required to
99 be ± 600 nT. To better observe the abundant low-frequency plasma waves in the GEO orbit, the
100 bandwidth of FGM is required to be between DC-7Hz, and the noise is $0.01\text{nT/Hz}^{1/2}$. According
101 to the requirements of measurement range and noise, the SNR of the instrument needs to reach
102 100 dB. The digital signal processing scheme can achieve a balance among digital resolution,
103 hardware resources, and reliability.

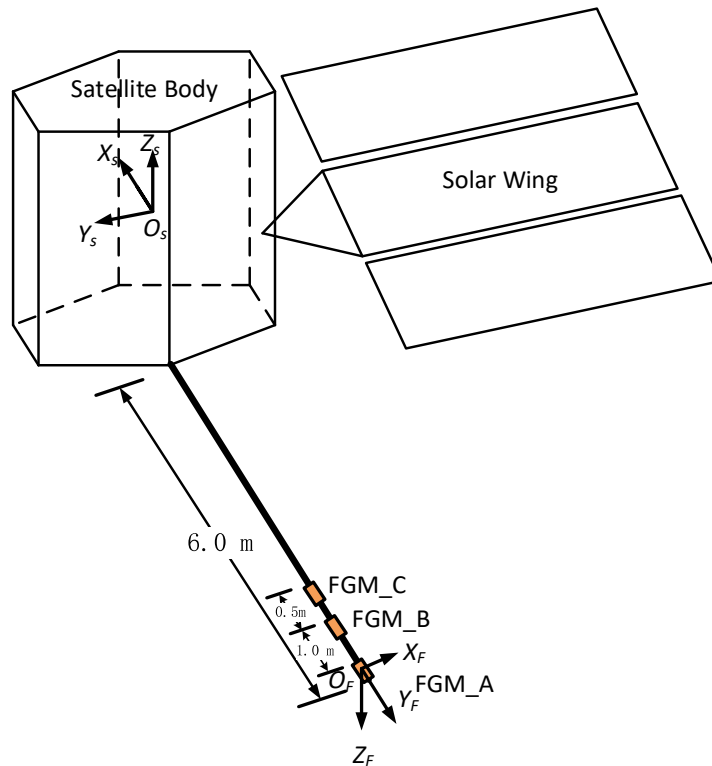
104 **3 Instrument Description**

105 The FY-4B FGM consists of three 3-axis fluxgate sensors. Each sensor owns a separate digital
106 signal processing electronic board. Three electronic boards are mounted in an electronic box.
107 Figure 1 shows a picture of the FY-4B FGM flight model. The interference from the satellite can
108 be better evaluated by the three fluxgate sensors, and this redundant design also improves the
109 overall reliability of the instrument.



110
 111 **Figure 1. The flight model of the FY-4B FGM includes three sensors and one electronic box.**
 112

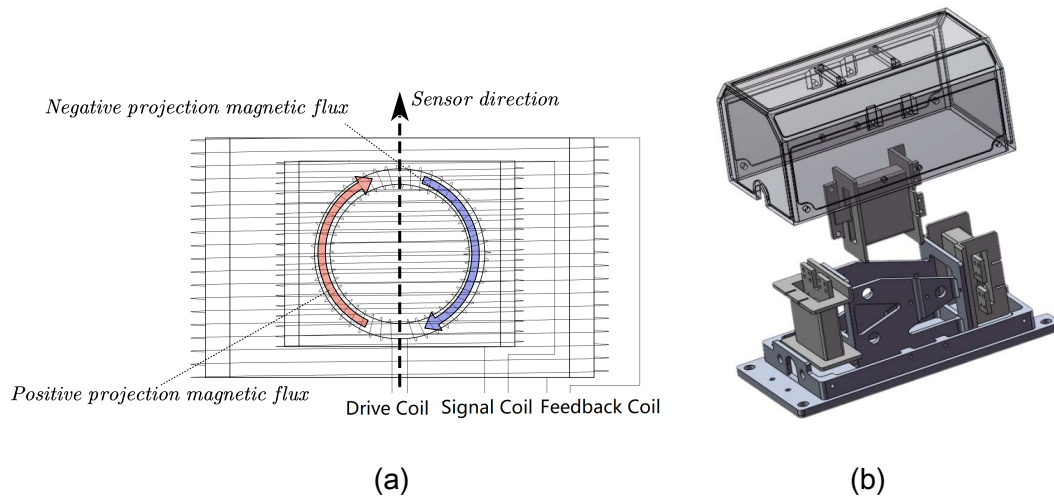
113 The sensors are mounted on a 6 m boom as shown in Figure 2. The +X of the FGM is aligned
 114 with the -Y axis of the satellite, the +Y axis of the sensor is aligned with the -X axis of the
 115 satellite, and the +Z axis of the sensor is aligned with the -Z axis of the satellite. The +Z of the
 116 satellite points to the earth. From April to September, the +X of the satellite points to the
 117 direction of flight, and the +Y of the FGM points to the west; from October to following March,
 118 the satellite roll over around the Z axis, with -X pointing to the direction of flight and +Y of the
 119 FGM pointing to the east.



120
 121 **Figure 2. The FGM sensors on the boom of FY-4B. The $O_s X_s Y_s Z_s$ is the FY-4B body**
 122 **coodiation, and the $O_F X_F Y_F Z_F$ is the FGM sensor coodiation.**

123 3.1 Sensor

124 Each single-axis fluxgate sensor is composed of three coils, including an excitation coil, a signal
 125 coil, and a feedback coil, see Figure 3(a), where the excitation coil is a spiral ring coil wrapped
 126 around a ring core made of high magnetic permeability material. The three single-axis sensors
 127 are mounted orthogonally to form a three-axis fluxgate sensor, and the internal structure of the
 128 sensor is shown in Figure 3(b). The magnetic field generated by the excitation current makes the
 129 core material magnetically saturated periodically. The signal coil has an annular magnetic flux
 130 inside, and the projection of the positive and negative magnetic flux in the axial direction of the
 131 signal coil is balanced. The superposition of the external magnetic field and the excitation field is
 132 constrained by the magnetic saturation of the core material, and the magnetic flux in the signal
 133 coil appears as a second harmonic signal at the excitation frequency, and the intensity of this
 134 signal is proportional to the external magnetic field.
 135



136

137

138 **Figure 3. The internal structure of the FGM sensor. (a) The structure of the fluxgate sensor**
 139 **and magnetic flux inside the ring core. (b) The orthogonal mounting layout of three-axis**
 140 **sensors.**

141 3.2 Electronics

142 Normal fluxgate signal processing includes a pre-amplifier, phase-sensitive demodulator,
 143 integrator, filters, and V-I amplifier. Figure 4 shows a block diagram of the digital signal
 144 processing circuit of the FGM. In this case, only the pre-amplifier and V-I amplifier are
 145 hardware analog circuits. The pre-amplified signal is digitally sampled at high-speed through 12-
 146 bit ADC. In FPGA, phase-sensitive demodulation, integrator, and filtering will be realized by
 147 software. Finally, the digital signal is converted into a voltage signal through 14bit DA and
 148 output to the V-I amplifier. The FGM measurement has two ranges, $\pm 600\text{nT}$ in orbit and
 149 $\pm 65000\text{nT}$ for the ground test, which are realized by switching the feedback resistance. To make
 150 the magnetic field detection stable when the board temperature changes, resistance with a
 151 temperature drift coefficient of 5ppm is used as the feedback resistance.

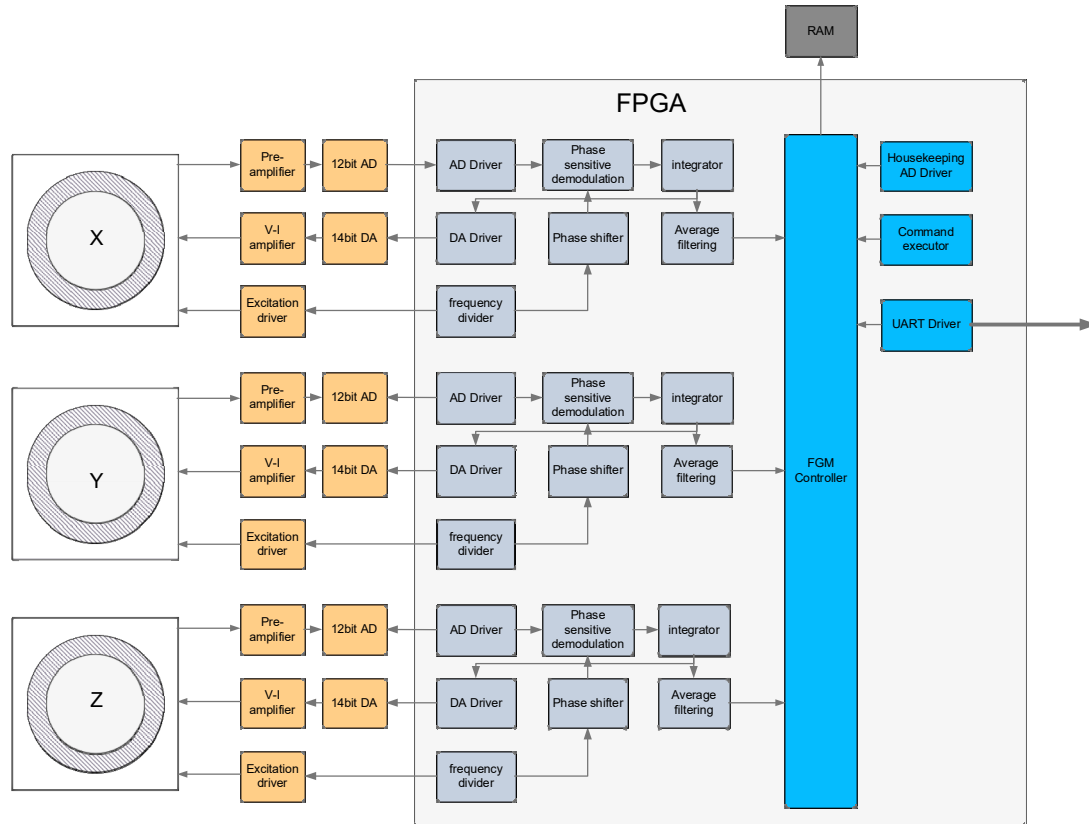


Figure 1. FGM circuit block diagram

152
153

154 3.3 Digital fluxgate signal processing of model

155 A digital fluxgate magnetometer is equivalent to an "ADC" device that converts a magnetic field
 156 into a digital value. Through modeling and simulation, the performance of the device can be
 157 confirmed, which is also the performance limit of the magnetometer. As far as possible, a real
 158 magnetometer signal can be modeled. When the excitation frequency is f_0 , the magnetic field is
 159 modulated by the sensor at $2f_0$. Since the excitation coil cannot be perfectly uniform, f_0 and its
 160 odd harmonics are also induced by the signal coil. So f_0 and $2f_0$ signals are used to simulate the
 161 sensor signal, as shown in Figure 5. The f_0 signal does not contain magnetic field information,
 162 but its oscillation modulation of the $2f_0$ signal is beneficial to signal detection.

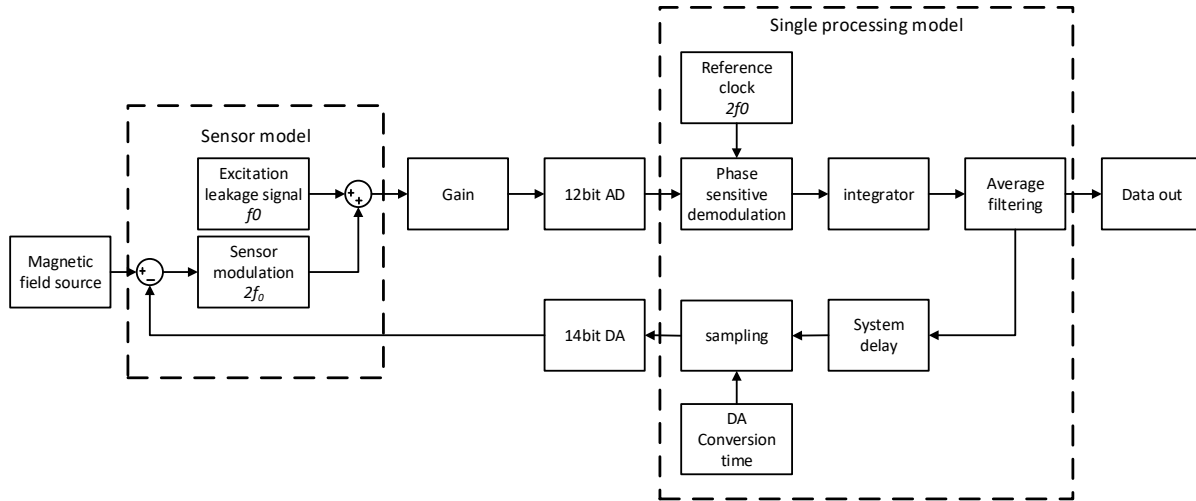
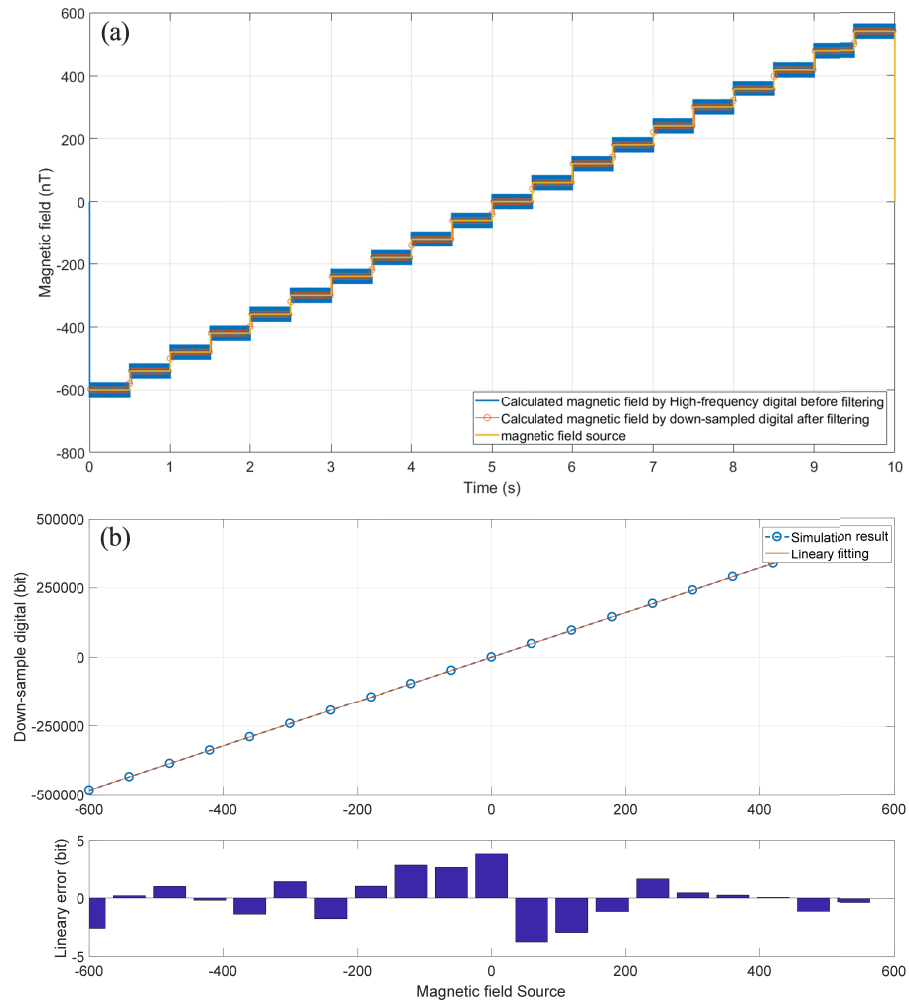


Figure 2. Simulation model of the fluxgate signal digital processing process

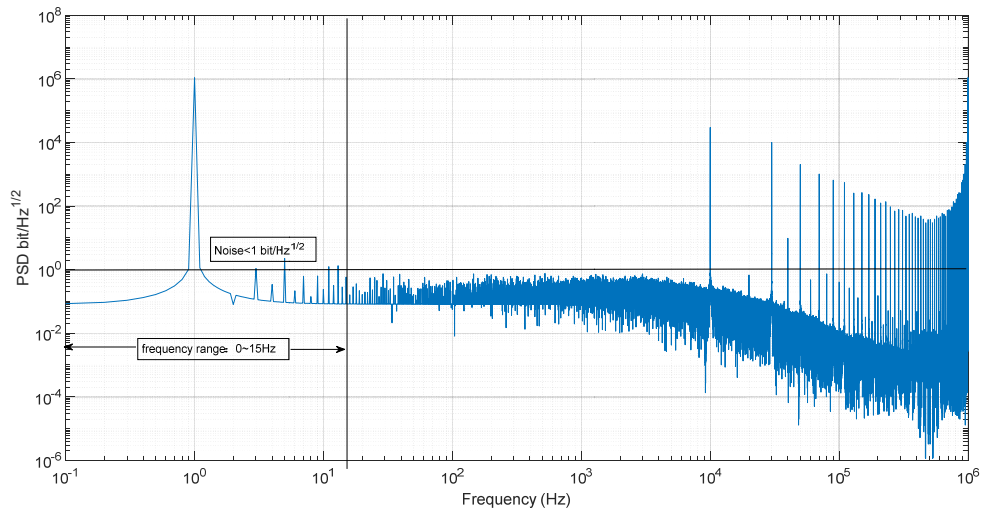
163
164
165

166 Figure 6 shows the simulated linear output of numerical processing. According to the output data
167 of 20bit digital resolution, the maximum linear error is about 4 LSB, which is equivalent to a
168 linear error of 5pT in a range of $\pm 600\text{nT}$. This linear error is negligible for the FY-4B magnetic
169 field detection. Using this model, we further obtain the SNR of digital signal processing. Figure
170 7 shows the PSD of a sinusoidal signal with 600nT amplitude before it is filtered and 30Hz
171 sampled after digital signal processing. According to the output data of 20bit digital resolution,
172 the noise is lower than $1 \text{ LSB}/\sqrt{\text{Hz}}$, and the corresponding magnetic field noise is $1\text{pT}/\sqrt{\text{Hz}}$. The
173 RMS noise in the band is better than 5 LSB in an effective bandwidth of 15Hz, and the SNR is
174 106dB after 30Hz sampled. Considering the linearity of digital signal processing and noise
175 simulation results, the effective digital resolution of FGM is 18-bit. Considering a certain margin
176 in the design, the magnetic field data of FGM can reach a 20-bit resolution.



177
178
179

Figure 3. The simulated linearity of the digital magnetometer model



180
181

Figure 4. Noise performance of the digital magnetometer model

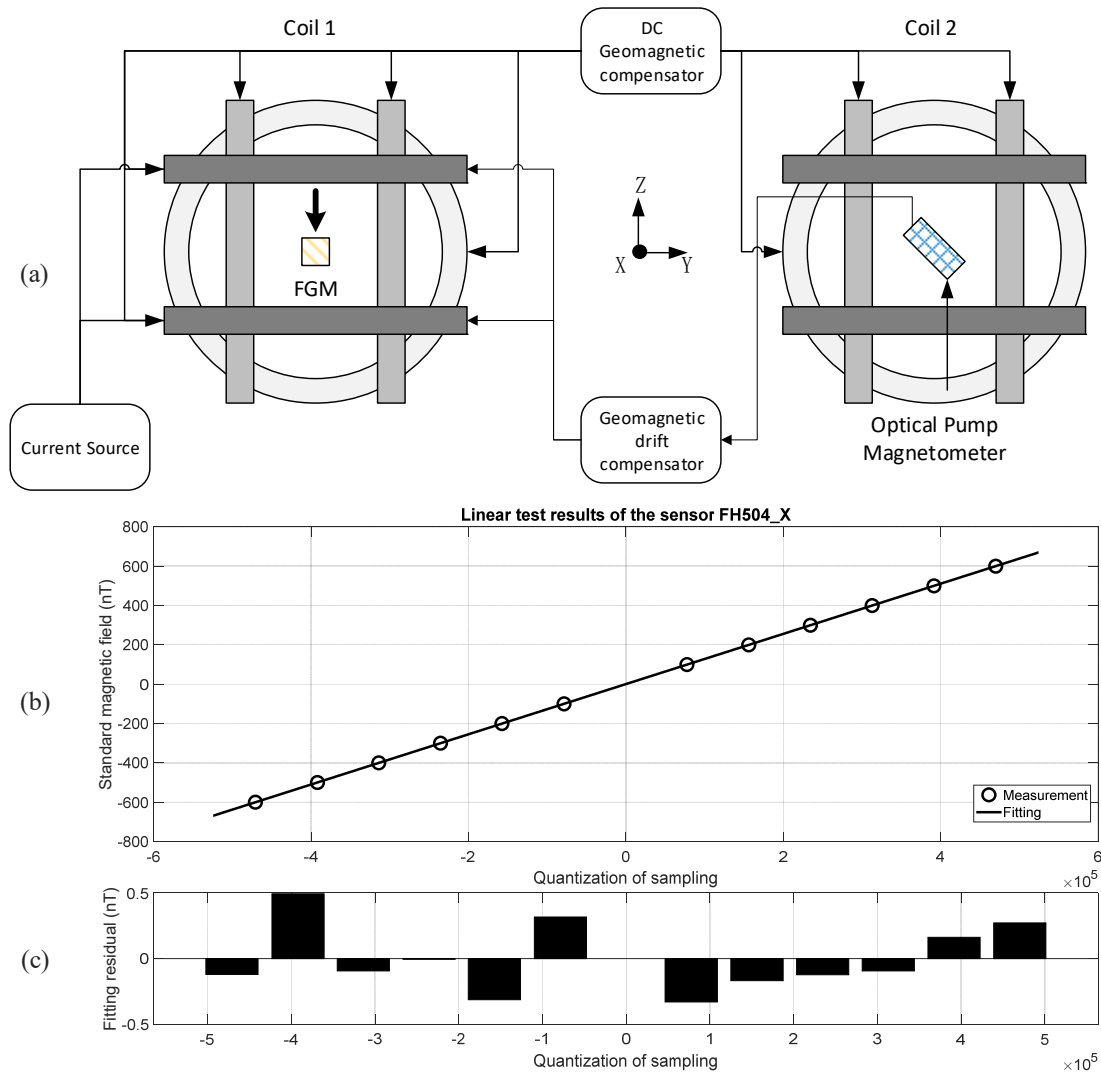
182

183 **4 Calibration**

184 4.1 Linearity test

185 The linearity test was carried out in a Helmholtz coil at the Fragrant Hills Weak Magnetic
186 Laboratory, National Institute of Metrology, China, which is the Chinese magnetic field
187 measurement benchmark. The Laboratory has been used to calibrate the magnetometer of
188 Yinghua-1 (Zhou et al., 2009) and CSES (Zhou et al., 2018). The test needs a Special coil system
189 (Figure 8(a)). Coil 1 compensates for the geomagnetic field in the XYZ direction, while coil 2
190 compensates for the geomagnetic field in the XY direction. The drift in the Z direction of the
191 geomagnetic field is approximately equal to the scalar magnetic field in coil 2. The optic-pump
192 magnetometer in coil 2 monitors this drift and compensates for the Z direction of coil 1. This
193 ensures the stability of the standard magnetic field in the Z-direction. This method can make the
194 magnetic field uncertainty no greater than 1nT.

195



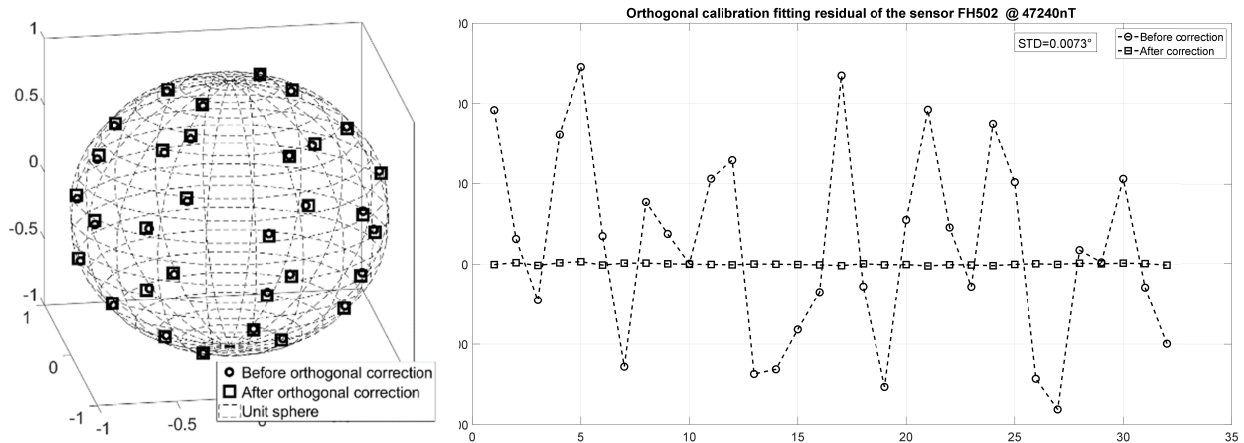
196
197 **Figure 8. Coil system for linearity test and the test result. (a) The coil system for the**
198 **linearity test consists of two triaxial Helmholtz coils, the main coil (left) is used to generate**
199 **the standard magnetic field and the other coil (right) is used to monitor the drift of the**
200 **geomagnetic field. (b)/(c) The maximum linear error is 0.5nT, which is within the**
201 **uncertainty of the test system**

202 The magnetic field in coil 1 can be calculated from the current and changed by the 100nT step.
203 The relationship between the magnetic field and measurement of the FGM can be fitted as a
204 straight line, and the ratio of fitting error to measurement range is the linearity of FGM. Figure
205 8(b) and (c) shows the linearity test result of the FGM A X-axis, and it reaches 0.038%.

206 4.2 Orthogonality test

207 In the orthogonality test, FGM works in the range of ± 65000 nT to improve the sensitivity to non-
208 orthogonality. A magnetic field of 50000nT is applied to coil 1 used in the linearity test. The
209 FGM sensor is rotating in the coil to measure the magnetic field of different relative directions.

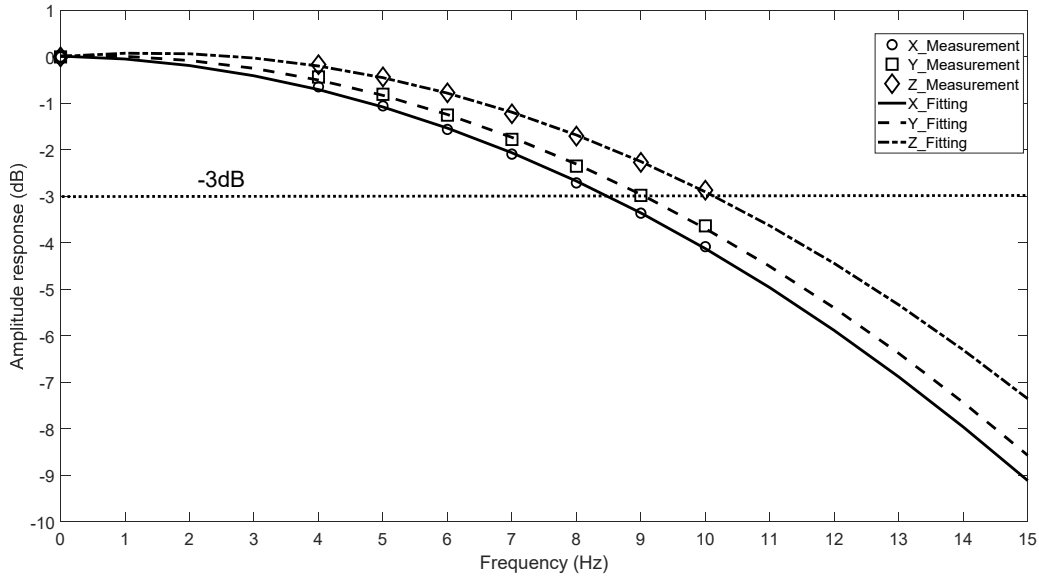
210 The orthogonal coefficients of the sensor are calculated by scalar equation (Zhou et al., 2018).
 211 Figure 9 shows the coverage of the measured magnetic field vector on a sphere, and the
 212 orthogonality calibration greatly reduces the scalar difference of FGM at about 50000nT. The
 213 uncertainty in the orthogonality is less than 0.01° . In the range of 600nT, the projection error
 214 caused by the non-orthogonal angle variation would not exceed 1nT after correction.



215
 216 **Figure 9. The angular distribution of the magnetic field in the Orthogonality test(left) and**
 217 **Comparison of scalar heading difference before and after orthogonality correction(right).**

218 4.3 Frequency response test

219 This test was also performed in the Helmholtz coil, which is used to compensate for the
 220 geomagnetic field and generate AC magnetic field from 4Hz to 10Hz, and the FGM
 221 measurement is recorded at the same time. Figure 10 shows the signal amplitude response at
 222 these frequencies. The -3db bandwidth of each component of FGM is above 7Hz. In a digital
 223 magnetometer, the amplification factor of the magnetic field affects the frequency response. The
 224 signal amplitude of each axis sensor and the corresponding amplification are manually optimized.
 225 So, the frequency response of each component is not the same as can be seen from the test results.

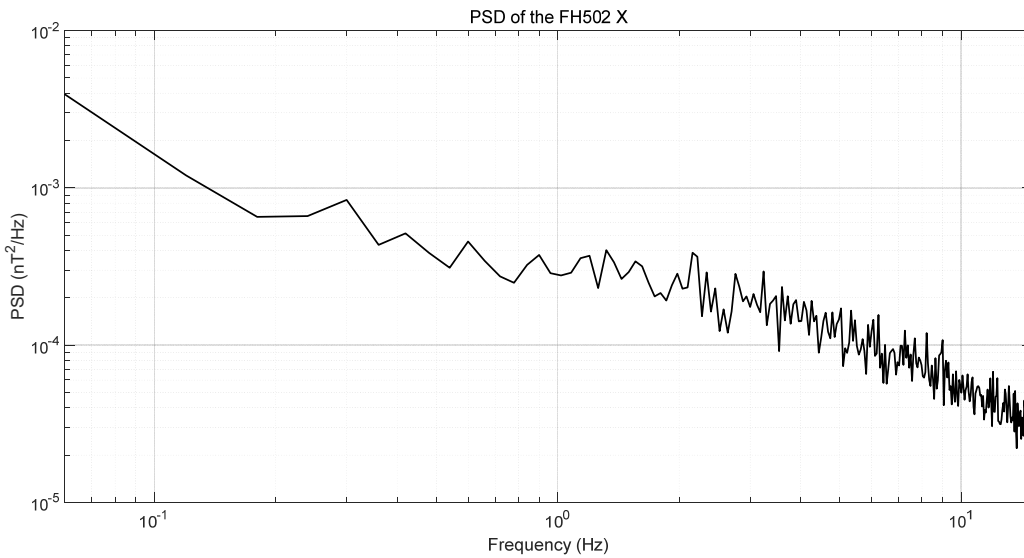


226
227
228

Figure 10. Frequency response of FGM A

229 4.4 Noise test

230 The noise test of FGM was carried out in a 600mm diameter and 2m length magnetic shield in
231 the weak magnetism laboratory of the National Space Science Center, CAS. Inside the magnetic
232 shield, the remanence can be less than 1 nT. It can effectively reduce external magnetic field
233 disturbances. Figure 11 shows the PSD curve of the noise test. The PSD of noise is lower than
234 that of $3 \times 10^{-4} \text{ nT}^2/\text{Hz}@1\text{Hz}$
235



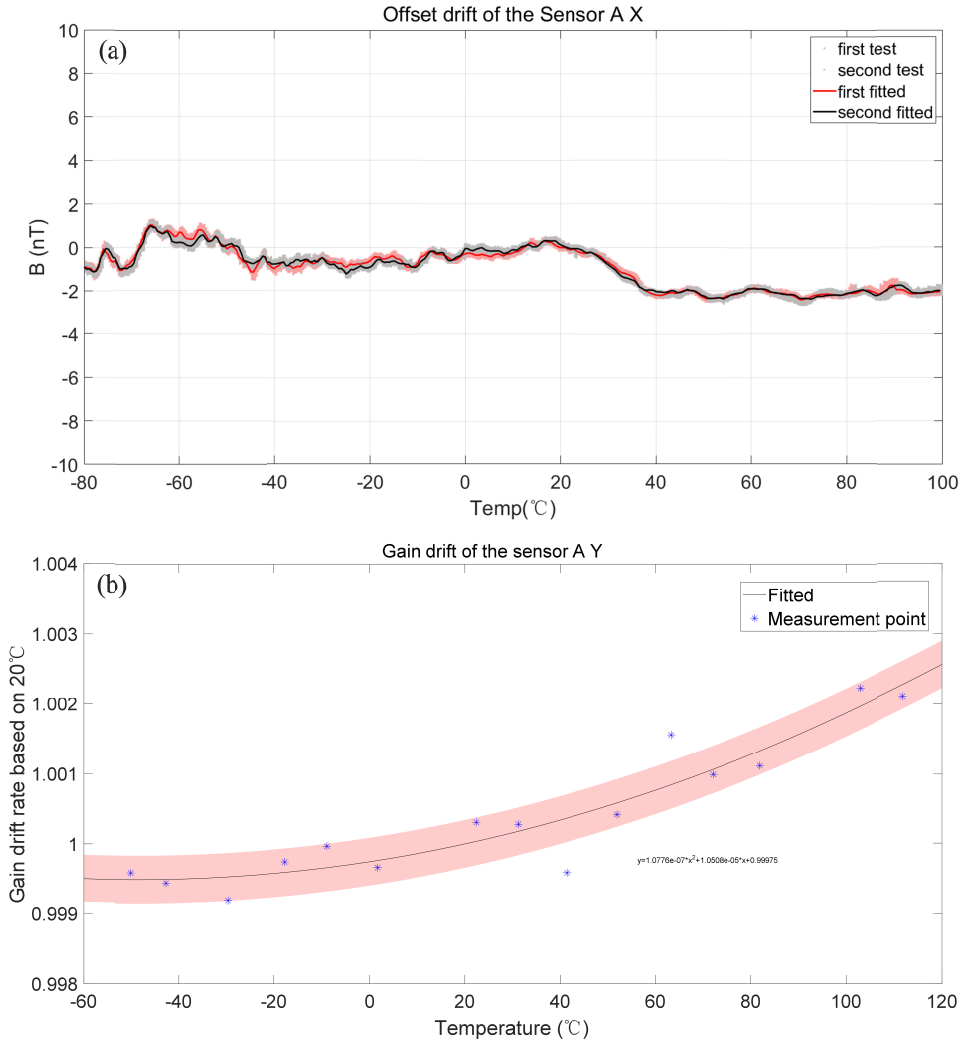
236
237

Figure 11. Noise PSD of FGMA X-component

238 4.5 Temperature drift test

239 In GEO orbit, solar illumination and Earth shadow alternate in a one-day cycle. So, the
240 temperature of the sensor changes in 24 hours, which is the main source affecting the
241 measurements. The sensor has passive thermal protection, according to the estimated
242 temperature range of $\pm 100^{\circ}\text{C}$. The temperature of the electronics box is relatively stable inside
243 the satellite, and the influence of the electronics temperature drift on the measurement can be
244 ignored for a signal processing system adopting a low-temperature drift feedback resistance.

245 The temperature calibration test was carried out in the laboratory in Yichang. The temperature
246 test cycle is 24 hours, simulating the process of in-orbit heating and cooling. Each sensor had a
247 two cycles test. Figure 12(a) below shows the temperature drift of the sensor offset. The
248 temperature drift of the offset for a fluxgate sensor in a wide temperature range is neither linear
249 nor monotonous. The offset temperature drift curve can be reproduced in the same process of
250 heating and cooling, even with some details. The gain temperature drift is mainly determined by
251 the thermal expansion of the coil materials and structure. It has good linearity and the change is
252 smooth. From the curves of figure 12(b), it can be seen that the drift rate of offset with
253 temperature is less than $0.1\text{nT}/^{\circ}\text{C}$ and the drift rate of gain with temperature is less than 50 ppm.



254
255
256

Figure 12. Temperature drift. (a) and (b) show the drift of offset and gain with the temperature of the sensor

257

4.6 Summary of the ground calibration

258
259

Through the ground calibration test, the FGM performance can be confirmed, as shown in Table 1.

260

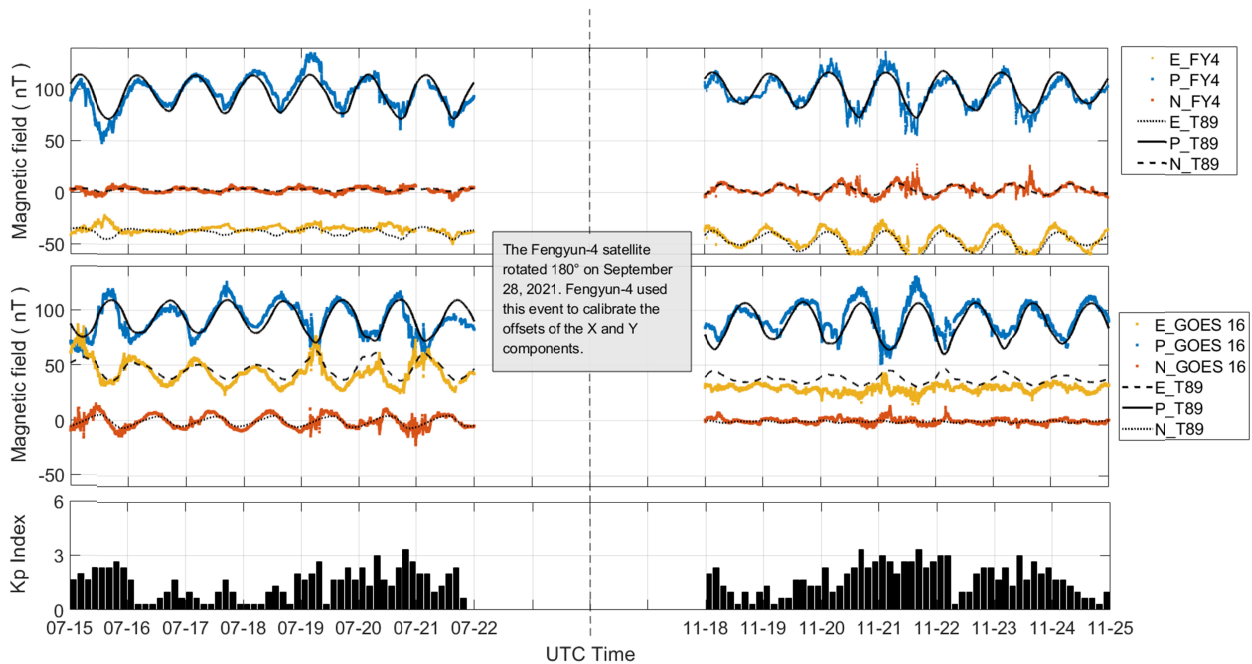
Table 1. FGM Performance

Measurement range	$\pm 600\text{nT}, \pm 65000\text{nT}$
Linearity	$\leq 0.04\%$
Frequency bandwidth	DC ~ 7Hz
Noise	$3 \times 10^{-4} \text{nT}^2/\text{Hz}@1\text{Hz}$
Orthogonality	$\leq 0.01^\circ$
Offset temperature stability	$\leq 0.1\text{nT}/^\circ\text{C}$
Gain temperature stability	$\leq 50\text{ppm}$

261 5. In-orbit preliminary results

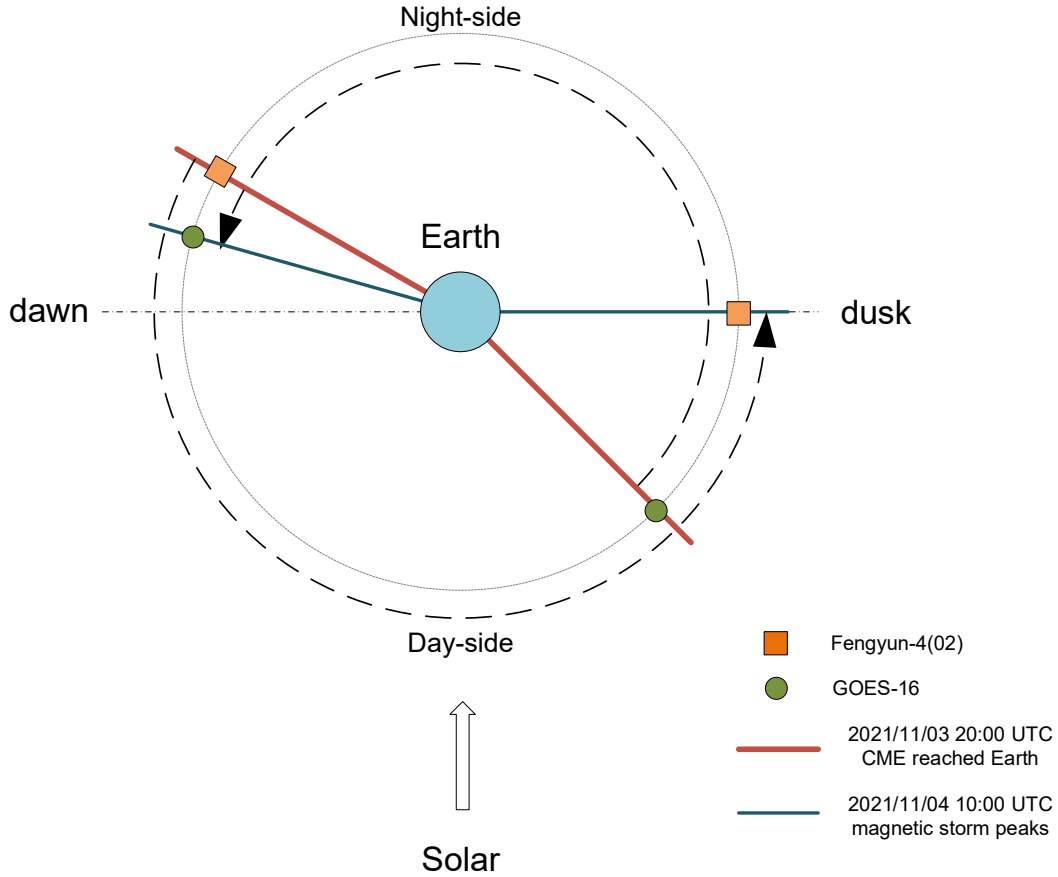
262 The three fluxgate sensors are installed near the top of the 6-meter boom on the FY-4B satellite.
 263 The influence of satellite remanent magnetism on the sensors has been greatly attenuated, and
 264 the static and dynamic interferences from the satellite can be effectively eliminated by the
 265 comparative analysis of the three sensors observation. The satellite rotates 180° around the Z
 266 axis near the spring and autumn equinoxes, while the X and Y components of the fluxgate sensor
 267 also rotate 180° with the satellite. This opportunity can be used to calibrate the Offset of the X
 268 and Y components. The calibration of the Z component offset is achieved by observation of the
 269 Alfvén wave events. Based on the known Offset of the X and Y components, the Z component
 270 offset can be calculated according to the Davis-Smith equation (Leinweber et al., 2008).

271 To verify the calibration results, the magnetic field data of FY-4B and GOES-16 satellites were
 272 compared in two 7-day periods before and after the rotating attitude of the satellite. FY-4B is
 273 located in GEO orbit at 123.4°E , and GOES-16 is located in GEO orbit at 75.2°W (Loto'aniu et
 274 al., 2019). The longitudinal difference between the two satellites is about 198° , and the magnetic
 275 fields observed by them are very different. For the comparison of two satellite observations, the
 276 T89 model is used as a reference, which is an empirical Earth's magnetospheric magnetic field
 277 (Tsyganenko, 1989). The model together with the IGRF model can reflect the distribution of the
 278 magnetic field within the magnetosphere. From Figure.13, T89 predictions (calculated by the Kp
 279 index from Matzka et al. (2021)) are generally consistent with the GOES-16 observations and
 280 can be used to evaluate the FY-4B observations. The comparison between the observations of
 281 FY-4B before and after the satellite rotation and the model is consistent, which indicates that the
 282 offset calibration is effective. The trend of magnetic field variation observed by FY-4B is
 283 consistent with the model, which indicates that FY-4B can correctly reflect the magnetic field
 284 variation in GEO orbit, just like the GOES-16 satellite.



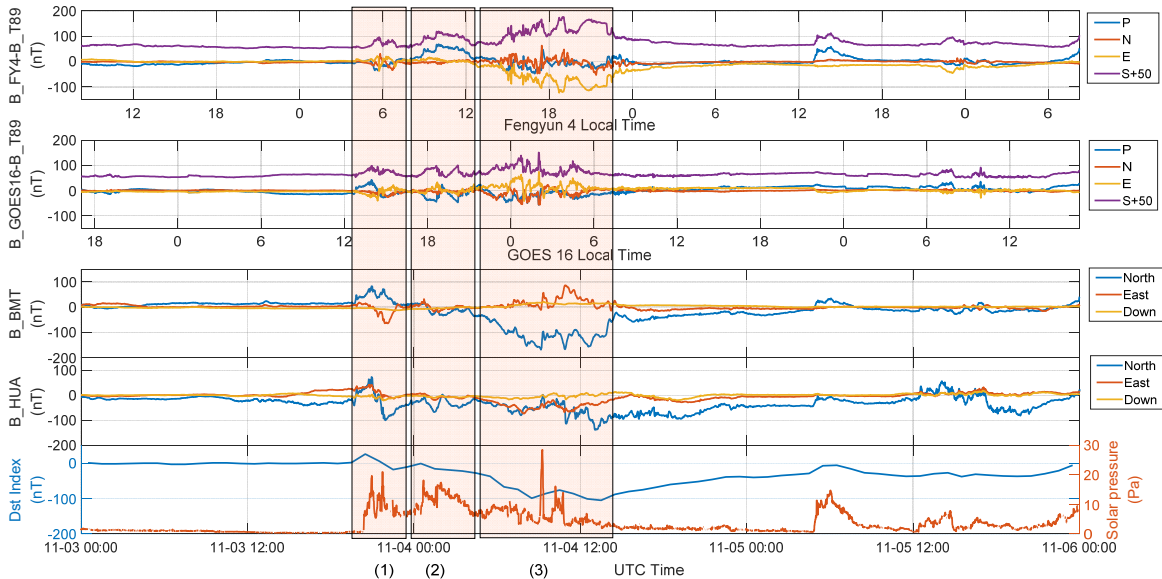
285
 286 **Figure 13. Comparison of magnetic field data from FY-4B and GOES-16 satellites with the**
 287 **T89 model, within two periods before and after September 28, respectively. The offset of**
 288 **the X and Y components of the magnetic field was calibrated during the satellite rotation**
 289 **maneuver on September 28.**

290
291 A stronger magnetic storm event occurred on November 4, 2021, and was observed by the FY-
292 4B satellite, GOES-16 satellite, and geomagnetic stations. The CME reached Earth on November
293 3, 2021, at ~20:00 UTC. According to the DST index(Kyoto doi:10.17593/14515-74000), the
294 magnetic storm entered the initial phase. According to the solar wind dynamic pressure, there
295 were two magnetopause compression processes in the initial phase. The main phase began at
296 about 04:00 UTC and peaks at 10:00 UTC the next day with a DST index of -100 nT. During this
297 process, the FY-4B satellite moved from the night side of the dawn terminator (4:00 local time)
298 to the dusk (18:00 local time); the GOES-16 satellite moved from the day side of the dusk
299 terminator (15:00 local time) to the night-side, and finally approached the dawn terminator (5:00
300 local time). Figure 14 shows the relative positions of the two satellites. Two geomagnetic
301 stations, BMT (40.3°N, 116.2°E) in Beijing and HUA (12.1°S, 75.3°W) in Peru, are close to the
302 longitudes of FY-4B and GOES16 satellites, respectively (Gjerloev, 2012). Figure 15 shows the
303 observations from November 3 to 6 including the magnetic storm. During the 8 hours of the
304 initial phase, FY-4B and GOES-16 satellites observed two obvious magnetic field enhancement
305 processes, the first time GOES-16 (dayside) had an obvious enhancement of about 50nT in the P
306 component, while the magnetic field disturbances of FY-4B (night side) appear in the 3
307 components. The second time FY-4B (dayside) had an enhancement of about 60 nT in the P
308 component and the GOES-16 satellite (night side) magnetic field disturbances in all three
309 components. When the magnetic storm then enters the main phase, a large number of charged
310 particles are injected into the inner magnetosphere, gradually forming a ring current, which was
311 first seen by GOES-16 located at midnight. FY-4B moved from near the subsolar point to dusk
312 and flew over the region of the ring current growth on the dusk side, thus observing the larger
313 magnetic field generated by the ring current. The disturbed earthward magnetic field was
314 observed on the FY-4B satellite, indicating that the ring current is already very close to the GEO
315 orbit, considering that FY-4B is located south of the magnetic equator. Meanwhile, the GOES-16
316 satellite flew from midnight to the dawn terminator, observing the magnetic field disturbance
317 earlier than FY-4B, and thereafter magnetic field was significantly less disturbed than that
318 observed by the FY-4B satellite, due to the weaker ring current on the dawn side. Similarly, the
319 magnetic field perturbation observed by HUA on the ground is also significantly weaker than
320 that observed by BMT. The evolution of the ring current in this magnetic storm is consistent with
321 the model description (e.g., Fok et al., 2001).



322
323
324

Figure 14. The location of FY-4B and GOES-16 satellites in GEO orbit during the magnetic storm



325
326
327
328
329

Figure 15. Observations of the magnetic field during the magnetic storm on November 4, 2021. The highlighted interval (1) is the first magnetopause compression in the initial phase. Interval (2) is the second magnetopause compression in the initial phase. Interval (3) is the main phase of the magnetic storm

330 **6 Conclusions**

331 The paper introduces the development, testing, and calibration of the FY-4B digital fluxgate
332 magnetometer. This payload achieves 20-bit digital resolution and 30Hz sampling in a range of
333 ± 600 nT, and the noise level is lower than 3×10^{-4} nT²/Hz @1Hz. The ground tests confirm FGM
334 performances meet the requirements of the FY-4 mission. After the in-orbit calibration, the
335 magnetic field observation of the FY-4B satellite is consistent with the GOES-16 satellite
336 observation and prediction by the magnetospheric magnetic field model. As demonstrated by the
337 observation in a typical magnetic storm, the FY-4B satellite magnetometer has the capability for
338 long-term magnetic field monitoring in the GEO orbit.

339 **Acknowledgments**

340 This work was supported by the National Key R&D Program of China (2021YFA0718600), and
341 the National Natural Science Foundation of China (41931073). We gratefully acknowledge the
342 SuperMAG collaborators (<https://supermag.jhuapl.edu/info/?page=acknowledgement>)

343 **Data Availability Statement**

344 The magnetic field data of FY-4B used in this paper is provided by the China National Satellite
345 Meteorological Center and can be obtained at <http://satellite.nsmc.org.cn/>. Full access to the data
346 requires an application after real-name registration. Geomagnetic station data can be accessed at
347 the SuperMag website. The geomagnetic indices used in this study can be found at
348 <https://doi.org/10.5880/Kp.0001> and <http://wdc.kugi.kyoto-u.ac.jp/wdc/Sec3.html> for Kp and Dst
349 respectively. And the solar wind dynamic pressure is available at <http://omniweb.gsfc.nasa.gov>.

350 **References**

- 351 Baumjohann, W., Matsuoka, A., Magnes, W., Glassmeier, K. H., Nakamura, R., & Al, E. (2010).
352 Magnetic field investigation of Mercury's magnetosphere and the inner heliosphere by
353 MMO/MGF. *Planetary & Space Science*, 58(1-2), 279-286.
354 <https://doi.org/10.1016/j.pss.2008.05.019>
- 355 Cheng, B. J., Zhou, B., Werner, M., Roland, L., & Andreas, P. (2018). High precision
356 magnetometer for geomagnetic exploration onboard the China Seismo-Electromagnetic Satellite.
357 *Science China: Technological Sciences*, 61(5), 659-668. [https://doi.org/10.1007/s11431-018-](https://doi.org/10.1007/s11431-018-9247-6)
358 [9247-6](https://doi.org/10.1007/s11431-018-9247-6)

- 359 Erik, B. P., Fritz, P., Jan, R. P., Merayo, J. M. G., Peter, B., & Nielsen, O. V. (1999). Digital
360 fluxgate magnetometer for the Astrid-2 satellite. *Measurement Science and Technology*, 10(11),
361 N124. <https://dx.doi.org/10.1088/0957-0233/10/11/402>
- 362 Fok, M.-C., Wolf R. A., Spiro R. W., and Moore T. E. (2001). A comprehensive computational
363 model of the Earth's ring current, *Journal of Geophysical Research*, 106, 8417-8424.
364 <https://doi.org/10.1029/2000JA000235>
- 365 Glassmeier, K. H., Auster, H. U., Heyner, D., Okrafka, K., Carr, C., Berghofer, G., et al. (2010).
366 The fluxgate magnetometer of the BepiColombo Mercury Planetary Orbiter. *Planetary and*
367 *Space Science*, 58(1), 287-299. <https://doi.org/10.1016/j.pss.2008.06.018>
- 368 Gjerloev, J. W. (2012). The SuperMAG data processing technique. *Journal of Geophysical*
369 *Research: Space Physics*, 117(A9). <https://doi.org/10.1029/2012JA017683>
- 370 Leinweber, H. K., Russell, C. T., Torkar, K., Zhang, T. L., & Angelopoulos, V. (2008). An
371 advanced approach to finding magnetometer zero levels in the interplanetary magnetic field.
372 *Measurement Science and Technology*, 19(5), 055-104. [https://dx.doi.org/10.1088/0957-](https://dx.doi.org/10.1088/0957-0233/19/5/055104)
373 [0233/19/5/055104](https://dx.doi.org/10.1088/0957-0233/19/5/055104)
- 374 Loto'aniu, T. M., Redmon, R. J., Califf, S., Singer, H. J., Rowland, W., Macintyre, S., et al.
375 (2019). The GOES-16 Spacecraft Science Magnetometer. *Space Science Reviews*, 215(4), 32.
376 <https://doi.org/10.1007/s11214-019-0600-3>
- 377 Matzka, J., Stolle, C., Yamazaki, Y., Bronkalla, O. and Morschhauser, A. (2021). The
378 geomagnetic Kp index and derived indices of geomagnetic activity. *Space Weather*, 19(5),
379 e2020SW002641. <https://doi.org/10.1029/2020SW002641>
- 380 Tsyganenko, N. A. (1989). A magnetospheric magnetic field model with a warped tail current
381 sheet. *Planetary and Space Science*, 37, 5-20.
382 <https://ui.adsabs.harvard.edu/abs/1989P&SS...37....5T>
- 383 Yang, J., Zhang, Z., Wei, C., Lu, F., & Guo, Q. (2017). Introducing the New Generation of
384 Chinese Geostationary weather Satellites, Fengyun-4. *Bulletin of the American Meteorological*
385 *Society*, 98(8),1637-1658. <https://doi.org/10.1175/BAMS-D-16-0065.1>
- 386 Zhang, T. L., Berghofer, G., Magnes, W., Delva, M., & Richter, I. (2007). MAG: The Fluxgate
387 Magnetometer of Venus Express. ESA special publication. SP 1295, 1-10.
- 388 Zhou, B., Zhao, H., Wang, J., Chen, S., & Jingxuan, Z. (2009). Martian Space Environment
389 Magnetic Field Investigation---High Accuracy Magnetometer. *Chinese Journal of Space Science*.
390 29(5), 467-474. <https://doi.org/10.11728/cjss2009.05.467>
- 391 Zhou, B., Yang, Y., Zhang, Y., Gou, X., et al. (2018). Magnetic field data processing methods of
392 the ChinaSeismo-Electromagnetic Satellite. *Earth and Planetary Physics*, 2(6), 455-461.
393 <https://doi.org/10.26464/epp2018043>